Real-time Imaging of Tumor-Cell Shedding and Trafficking in Lymphatic Channels

Katsuhiro Hayashi,[1,2,3] Ping Jiang,[1] Kensuke Yamauchi,[3] Norio Yamamoto,[3] Hiroyuki Tsuchiya,[3] Katsuro Tomita,[3] A.R. Moossa,[2] Michael Bouvet,[2] and Robert M. Hoffman[1,2]

[1]AntiCancer, Inc.; [2]Department of Surgery, University of California, San Diego, San Diego, California; and [3]Department of Orthopaedic Surgery, School of Medicine, Kanazawa University, Kanazawa, Ishikawa, Japan

Abstract

In the present report, we show real-time imaging of cancer cell trafficking in lymphatic vessels. Cancer cells labeled with both green fluorescent protein (GFP) in the nucleus and red fluorescent protein (RFP) in the cytoplasm or with GFP only or RFP only were injected into the inguinal lymph node of nude mice. The labeled cancer cells trafficked through lymphatic vessels where they were imaged via a skin flap in real time at the cellular level until they entered the axillary lymph node. The bright fluorescence of the cancer cells and the real-time microscopic imaging capability of the Olympus OV100 small-animal imaging system enabled imaging of the trafficking cancer cells in the lymphatics. Using this imaging strategy, two different cancer cell lines, one expressing GFP and the other expressing RFP, were simultaneously injected in the inguinal lymph node. Fluorescence imaging readily distinguished the two color-coded cell lines and their different abilities to survive in the lymphatic system. Using this imaging technology, we also investigated the role of pressure on tumor-cell shedding into lymphatic vessels. Pressure was generated by placing 25- and 250-g weights for 10 s on the bottom surface of a tumor-bearing footpad. Tumor cell fragments, single cells, and emboli shed from the footpad tumor were easily distinguished with the labeled cells and OV100 imaging system. Increasing pressure on the tumor increased the numbers of shed cells, fragments, and emboli. Pressure also deformed the shed emboli, increasing their maximum major axis. Imaging lymphatic trafficking of cancer cells can reveal critical steps of lymph node metastasis. [Cancer Res 2007;67(17):8223–8]

Introduction

The major pathways of cancer cell dissemination are the lymphatic system and the circulatory system. However, the role of the lymphatic system in cancer metastasis is less well understood compared with the circulatory system (1).

Lymphangiogenesis is associated with an increased incidence of lymph node metastasis. Tumor-secreted cytokines, such as vascular endothelial growth factor (VEGF)-C and VEGF-D, bind to VEGF receptors on lymphatic endothelial cells and induce proliferation of new lymphatic capillaries (2, 3). However, despite its importance in lymphatic metastasis, cancer cell trafficking in lymphatic vessels, including entrance to the targeted lymph node, has been insufficiently investigated. Some studies suggest that the trafficking of tumor cells to lymph nodes resembles the normal migration of dendritic cells and that they follow a chemokine gradient (4). Tumor cells that express certain types of chemokine receptors are more likely to metastasize to the lymph node. A promising approach to the further understanding of trafficking of cancer cells in lymphatics is imaging.

Recently, *in vivo* imaging has been adapted to visualize normal cell trafficking in lymph nodes (5, 6). von Andrian and Mempel (7) and Halin et al. (8) have developed fluorescence visualization of lymphocyte trafficking, cell migration, and cell-cell interaction in lymph nodes using intravital microscopy. Stoll et al. (9) visualized T cells interacting with dendritic cells in lymph nodes using multicolor fluorescence. Dadiani et al. (10) imaged breast cancer emboli clustering at a lymphatic vessel junction. However, trafficking of cancer cells in lymphatic vessels was not investigated in these studies.

Interstitial fluid pressure (IFP) in tumors and in the peritumoral extracellular matrix correlates with lymphatic flow and tumor migration (11). Young et al. (12) reported in 1950 that the hydrostatic pressure of tumors is often increased, and now it is well known that the IFP of most solid tumors is increased, such as breast cancer, melanoma, head and neck cancer, and colorectal cancer (13–17).

The mechanisms of the increased tumor IFP are not well understood. Blood vessel leakiness, lymph vessel abnormalities, interstitial fibrosis, and a contraction of the interstitial space mediated by stromal fibroblasts are possible causes (18). Tumor blood vessels and lymphatic vessels are often structurally and functionally abnormal. These abnormalities can cause hypertension within the tumor. An imbalance in molecular factors regulating vessel growth and maturation as well as compressive mechanical forces generated by proliferating cancer cells could lead to vessel abnormality (19, 20).

Clinically, several studies have indicated that high IFP in the tumor is correlated with poor prognosis (15, 21, 22). Elinar et al. reported that high central tumor IFP was associated with the development of pulmonary and lymph node metastases in a melanoma xenograft mouse model (23). Increased IFP may decrease transcapillary transport and uptake of drugs into tumors, which are also factors for poor prognosis (18).

We have previously described real-time imaging of trafficking of tumor cells in blood vessels using fluorescent proteins (24, 25). We now aim to study the other main conduit for cancer cell trafficking, the lymphatic system. We report here the development of fluorescence real-time imaging of lymphatic trafficking at the cellular and subcellular levels. Dual-color fluorescent cancer cell lines expressing green fluorescent protein (GFP) in the nucleus and red fluorescent protein (RFP) in the cytoplasm served in a highly sensitive whole-mouse imaging system that was used.

Note: Supplementary data for this article are available at Cancer Research Online (http://cancerres.aacrjournals.org/).

Requests for reprints: Robert M. Hoffman, AntiCancer, Inc., 7917 Ostrow Street, San Diego, CA 92111-3604. Phone: 858-654-2555; Fax: 858-268-4175; E-mail: all@anticancer.com.

©2007 American Association for Cancer Research.

doi:10.1158/0008-5472.CAN-07-1237

With this new imaging technology, we studied three phenomena related to cancer cell trafficking in lymphatics: (*a*) trafficking of cancer cells to lymph nodes; (*b*) differential survival of cancer cell types in lymphatic channels; and (*c*) increasing tumor pressure increases tumor-cell shedding and trafficking in the lymphatics, which may account for poor prognosis of patients with high IFP.

Materials and Methods

Production of RFP or GFP retroviral vector. For RFP retrovirus production, the *Hin*dIII/*Not*I fragment from pDsRed2 (Clontech Laboratories, Inc.), containing the full-length *RFP* cDNA, was inserted into the *Hin*dIII/*Not*I site of pLNCX2 (Clontech Laboratories) containing the neomycin resistance gene. For GFP retrovirus production, the pLEIN retroviral vector (Clontech Laboratories) expressing enhanced GFP and the neomycin resistance gene on the same bicistronic message was used. PT67, an NIH3T3-derived packaging cell line (Clontech Laboratories) expressing the 10A1 viral envelope, was cultured in DMEM (Irvine Scientific) supplemented with 10% heat-inactivated fetal bovine serum (FBS; Gemini Bio-Products). For vector production, PT67 packaging cells, at 70% confluence, were incubated with a precipitated mixture of LipofectAMINE reagent (Life Technologies, Inc.) and saturating amounts of pLNCX2-DsRed2 plasmid for 18 h. Fresh medium was replenished at this time. The cells were examined by fluorescence microscopy 48 h posttransduction. For selection of a clone producing high amounts of RFP retroviral vector (PT67-DsRed2), the cells were cultured in the presence of 200 to 1,000 μg/mL G418 (Life Technologies) for 7 days. The isolated packaging cell clone was termed PT67-DsRed2.

Production of histone H2B-GFP vector. The histone *H2B* gene has no stop codon (26), which enables the ligation of the *H2B* gene to the coding region of the *GFP* gene (Clontech Laboratories). The histone *H2B-GFP* fusion gene was then inserted at the *Hin*dIII/*Cal*I site of the pLHCX (Clontech Laboratories), which has the hygromycin resistance gene. To establish a packaging cell clone producing high amounts of histone H2B-GFP retroviral vector, the pLHCX histone H2B-GFP plasmid was transfected in PT67 packaging cells using the same methods described above for PT67-DsRed2. The transfected cells were cultured in the presence of 200 to 400 μg/mL hygromycin (Life Technologies) for 15 days to establish stable PT67 H2B-GFP packaging cells.

Fluorescent protein–gene transduction of cancer cells. Cancer cells were labeled with RFP or GFP or RFP and H2B-GFP. Clones expressing RFP or GFP were initially established. In brief, cancer cells were incubated with a 1:1 precipitated mixture of retroviral supernatants of PT67-RFP cells or PT67-GFP cells and RPMI 1640 (Irvine Scientific) containing 10% FBS for 72 h. Fresh medium was replenished at this time. Cells were harvested with trypsin/EDTA 72 h posttransduction and subcultured at a ratio of 1:15 into selective medium, which contained 200 μg/mL G418. The level of G418 was increased stepwise up to 800 μg/mL. For double-labeling with RFP and H2B, RFP-expressing cancer cells were isolated with cloning cylinders (Bel-Art Products) using trypsin/EDTA and amplified by conventional culture methods. For establishing dual-color cancer cells, the RFP-expressing cells were then incubated with a 1:1 precipitated mixture of retroviral supernatants of PT67 H2B-GFP cells and culture medium. To select the double transformants, cells were incubated with hygromycin 72 h after transfection. The level of hygromycin was increased stepwise up to 400 μg/mL.

Mouse model for imaging real-time trafficking of cancer cells in lymphatic vessels in experimental metastasis. Fluorescent protein–expressing cancer cells were injected into the inguinal lymph node. Nude mice were anesthetized with a ketamine mixture (10 μL ketamine HCL, 7.6 μL xylazine, 2.4 μL acepromazine maleate, and 10 μL H_2O) via s.c. injection. An arc-shaped incision was made in the abdominal skin from the axillary to the inguinal region. The s.c. connective tissue was separated to free the skin flap without injuring the lymphatic vessel. Mice were laid flat and the skin flap was spread and fixed on the flat stand (Fig. 1*A*). The axillary lymph node was exposed from the inner side or the skin side. HT-1080 dual-color cells (5×10^4) in 10 μL were injected into the center of the inguinal lymph node. To increase contrast, 5 μL of PBS containing 5×10^4 RFP-expressing cancer cells were injected along with 5 μL of FITC-dextran (molecular weight, 2×10^6; Sigma-Aldrich). Images were acquired as described below with the Olympus OV100 small-animal imaging system. A total of 10 mice were used in this study.

Simultaneous imaging of cancer cells color-coded with GFP or RFP in lymphatic vessels and lymph nodes. To simultaneously compare the behavior of two cell lines in the same lymphatic vessel or lymph node, a mixture of 143B-GFP human osteosarcoma and B16-RFP murine melanoma cell lines was injected in the inguinal lymph node using the same technique as described above. Cells (5×10^5) of each cell line were mixed in a total of 10-μL PBS. The color-coded cancer cells in the lymphatic and inguinal

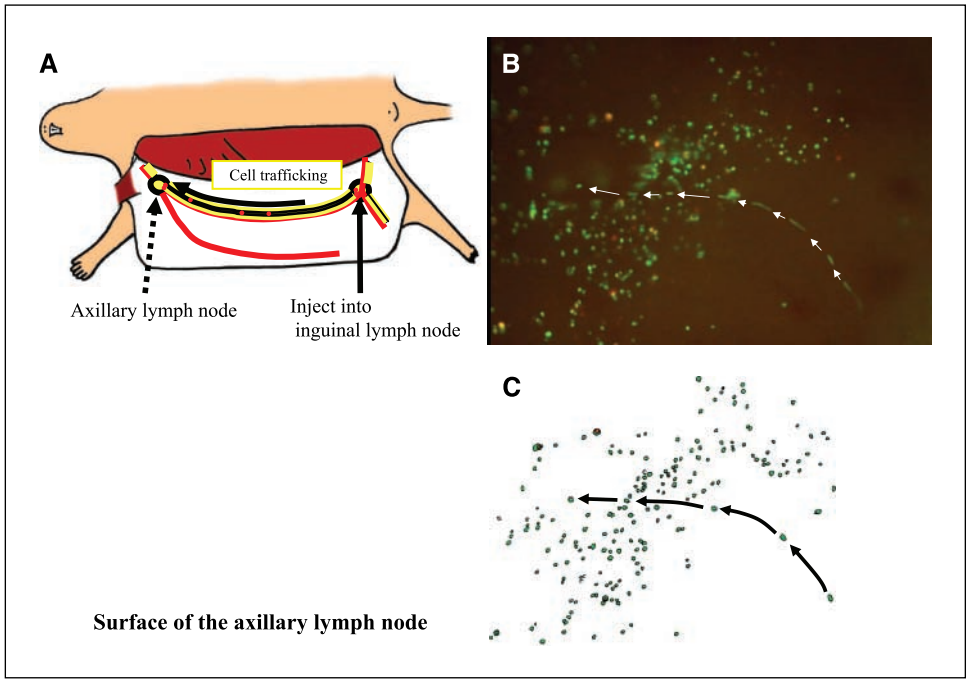

Figure 1. Experimental model of lymph node metastasis: cancer cells homing to the axillary lymph node after injection in the inguinal lymph node. *A,* dual-color HT-1080 human fibrosarcoma cells were injected into the inguinal lymph node. Nude mice were anesthetized and an arc-shaped incision was made in the abdominal skin from the axillary to the inguinal region. The s.c. connective tissue was separated to free the skin flap without injuring the lymphatic. The skin flap was spread and fixed on the flat stand. The axillary lymph node was exposed. *B,* cancer cells entering the axillary lymph node via the afferent lymph duct. A total of 10-μL medium containing 5×10^4 HT-1080 dual-color cells was injected into the center of the inguinal lymph node. *C,* schematic of (*A*).

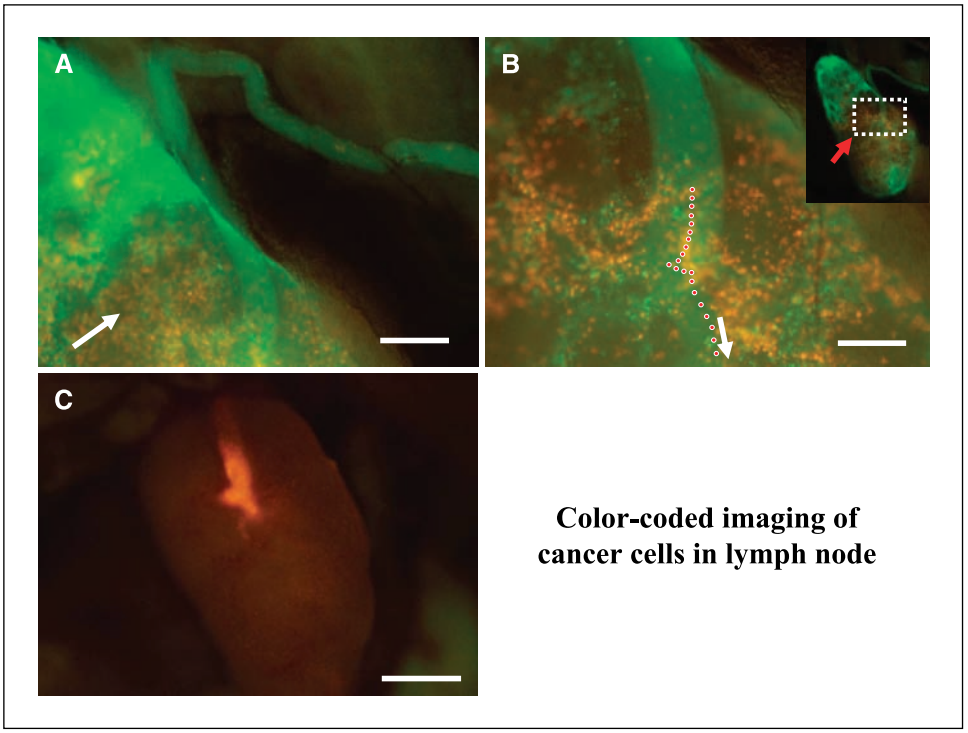

Figure 2. Simultaneous dual-color imaging of lymphatic structure and trafficking cancer cells. To simultaneously observe lymphatic structure and trafficking cancer cells, 5 μL containing 5×10^4 XPA1-RFP human pancreas cancer cells were injected along with 5 μL of FITC-dextran (molecular weight, 2×10^6). *A,* FITC-dextran (*green*) shows structure of the lymphatic and axillary lymph node. FITC-dextran permeates the lymph node, enabling visualization of the germinal center. Note the cancer cells arresting in the subcapsular sinus just after entrance to the lymph node (*arrow*). *Bar*, 500 μm. *B,* single-cell motion at the junction of afferent lymph duct and subcapsular sinus of the lymph node. *White arrow*, direction of cancer-cell trafficking. *Inset,* low magnification of whole lymph node as also seen in (*A*). *Red arrow*, where high magnification image of (*B*) was obtained. *Bar,* 200 μm. *C,* XPA1-RFP cells (5×10^5) were injected in the inguinal lymph node, and the axillary lymph node was imaged 7 d later. *Bar*, 1 mm.

lymph node were observed with the OV100 and images were taken on days 0 and 2. A total of 10 mice were used in this study.

Mouse model for imaging spontaneous shedding of tumor cells into lymphatic vessels. HT-1080 dual-color cells (2×10^6) in 20 μL were injected into the nude mouse footpad. Four weeks later, mice were anesthetized with the ketamine mixture via s.c. injection. Mice were laid in the prone position and the legs were fixed without stimulation of the tumor. A 2-cm straight incision was made in the ipsilateral popliteal region. The popliteal lymph node and lymphatic were exposed without injuring them. Shed tumor cells in the lymphatic vessel were imaged with the OV100.

Effect of pressure on tumor-cell shedding into lymphatic vessels. Pressure was generated by 25- and 250-g weights for 10 s each on the bottom surface of the tumor-bearing footpad to increase the internal pressure of the tumor. A cylindrical weight with a 10-mm diameter (78.5 mm^2) was used for the stimulation. After stimulation, cancer cell trafficking was imaged at video rate with the OV100 system at ×100 magnification for 1 min. The numbers of cell fragments, single cells, and emboli were counted by reviewing the saved video file. The major axis length of the largest embolus in each experiment was also measured. A total of 10 mice were used in this study. Statistical analysis was done using the two-tailed paired Student *t* test.

Cellular and subcellular imaging in live mice. The Olympus OV100 Small-Animal Imaging System (Olympus Corp.), containing an MT-20 light source (Olympus Biosystems) and DP70 charge-coupled device camera (Olympus), was used for subcellular imaging in live mice. The optics of the OV100 fluorescence imaging system have been specially developed for macroimaging as well as microimaging with high light-gathering capacity. The instrument incorporates a unique combination of high numerical aperture and long working distance. Four individually optimized objective lenses, parcentered and parfocal, provide a 105-fold magnification range for seamless imaging of the entire body down to the subcellular level without disturbing the animal. The OV100 has the lenses mounted on an automated turret with a high magnification range of ×1.6 to ×16 and a field of view ranging from 6.9 to 0.69 mm. The optics and antireflective coatings ensure optimal imaging of multiplexed fluorescent reporters in small animals. High-resolution images were captured directly on a PC (Fujitsu Siemens). Images were processed for contrast and brightness and analyzed with the use of Paint Shop Pro 8 and Cell^R (Olympus Biosystems).

Mice. Athymic *nu/nu* nude mice were kept in a barrier facility under HEPA filtration. Mice were fed with autoclaved laboratory rodent chow (Tecklad LM-485, Western Research Products). All animal studies were conducted in accordance with the principals and procedures outlined in the NIH Guide for the Care and Use of Laboratory Animals under assurance no. A3873-1.

Results and Discussion

Dynamic subcellular imaging of trafficking of cancer cells in lymphatic vessels in live mice (experimental model). We observed cell trafficking in lymphatics after injection of the tumor cells in the inguinal lymph node (Fig. 1*B* and *C*; see Supplementary Movie 1). With FITC-dextran labeling of the lymphatics, we could see both the lymphatic structure and the cancer cell trafficking (Fig. 2*A*). Cancer cells were imaged flowing in the center of the duct (see Supplementary Movie 2). At the junction of the afferent lymph duct and subcapsular sinus of the lymph node, the cancer cells disseminated by avoiding attachment to the lymphatic vessel wall (Fig. 2*B*). However, 7 days after injection, a tumor mass was occasionally observed at the junction (Fig. 2*C*). The junction seemed to be a focal point in lymph node metastasis.

Simultaneous imaging of cancer cells color coded with GFP or RFP in lymphatic vessels and lymph nodes. There was no significant difference in cell trafficking between the human 143B-GFP osteosarcoma cell line and the murine B16-RFP melanoma cell line. Both cell types were easily distinguished by GFP and RFP expression. After injection, both cell types were arrested around the junction of the afferent lymph duct and the lymph node (Fig. 3*B*). On day 2, 143B-GFP cells almost disappeared due to their decreased viability in the lymphatic and lymph node. B16-RFP cells remained in the lymph node and could proliferate (Fig. 3*C*). Using GFP and RFP makes it possible to simultaneously observe the differential survival of two cell lines in the same lymph node or vessel (27).

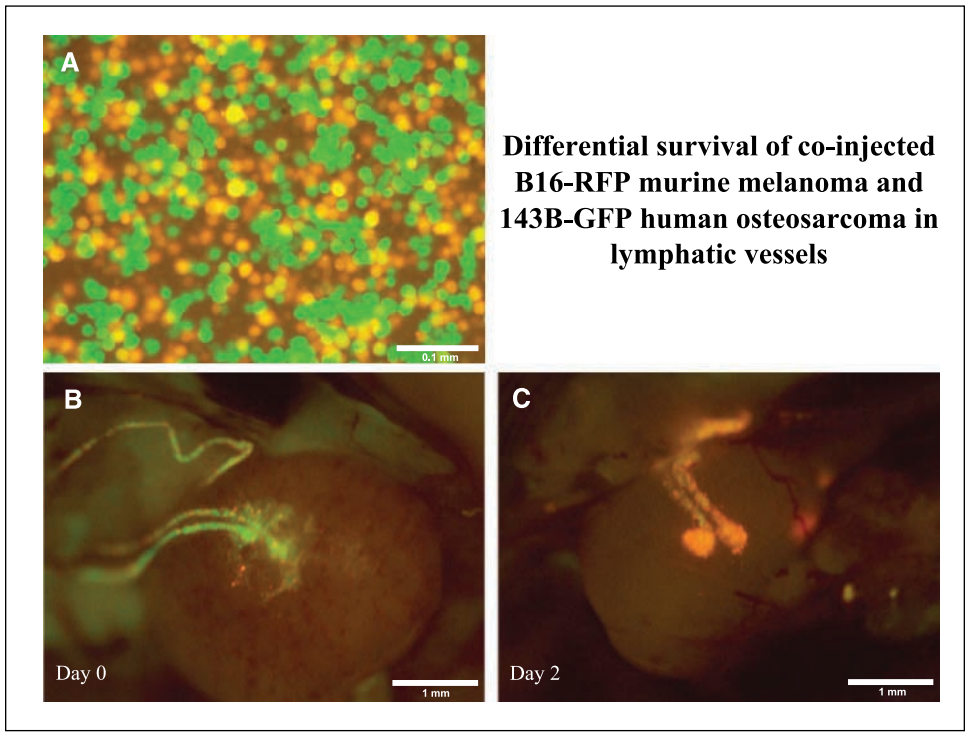

Figure 3. Simultaneous imaging of color-coded cell lines in the same lymph node. 143B-GFP human osteosarcoma and B16-RFP murine melanoma cell lines were injected in the inguinal lymph node using the same techniques as described above. *A,* equal cell number of each line was confirmed under fluorescence microscopy before injection. *B,* after injection, cells arrested around the junction of the afferent lymph duct and lymph node. *C,* on day 2, 143B-GFP cells almost disappeared due to poor survival in the lymph node whereas B16-RFP cells remained viable. *Bar*, 100 μm (*A*); 1 mm (*B* and *C*).

Dynamic subcellular imaging of trafficking of cancer cells in lymphatic in live mice (spontaneous model). Real-time trafficking of HT-1080 dual-color cell was observed in the popliteal lymphatic (Fig. 4*A–D*). Most of the cells were fragmented and appeared single color in the lymphatic, suggesting that most of the cancer cells already had fragmented before entering the peritumoral lymphatic and lymph flow. There were few living cells in the lymph duct.

Shedding of trafficking cancer cells in lymphatic as function of pressure. Cell fragments, single cells, and emboli were easily distinguished with the dual-color HT-1080 cell line and the OV100 imaging system. With 25-g stimulation of the footpad

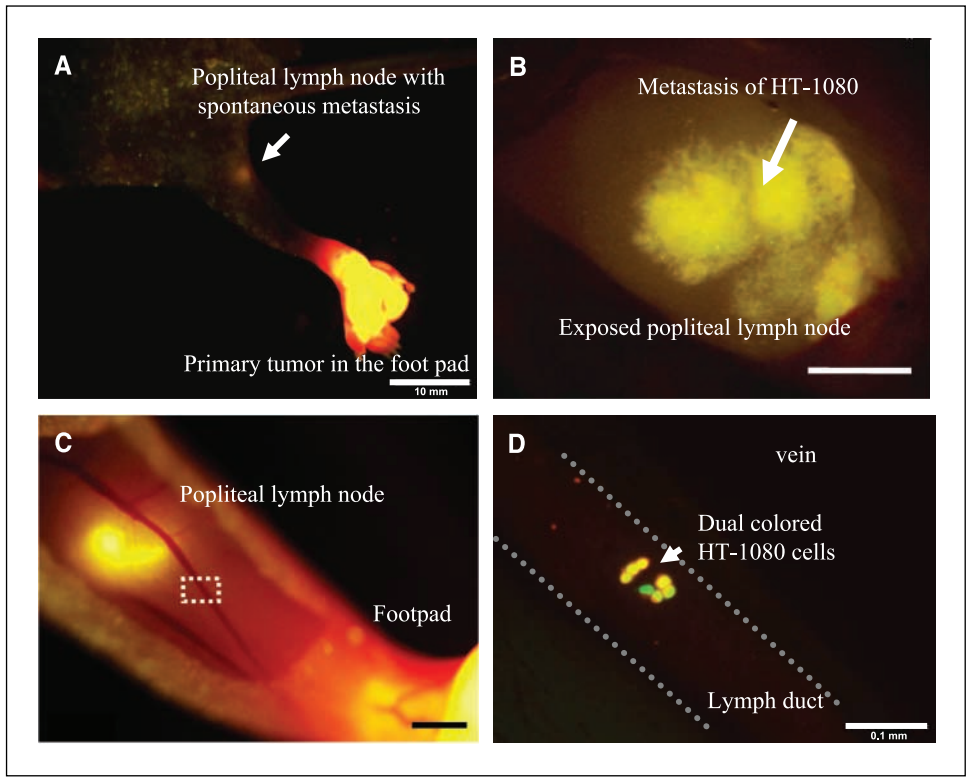

Figure 4. Footpad spontaneous metastasis model. *A*, dual-color HT-1080 cells expressing RFP in the cytoplasm and H2B-GFP in the nucleus were injected into the footpad. Four weeks later, mice were laid in the prone position and the primary tumor and popliteal lymph node metastasis were observed by whole-body fluorescence imaging with the Olympus OV100. *B*, fluorescence image of exposed popliteal lymph node as seen noninvasively in (*A*). Dual-color HT-1080 cells metastasized to the lymph node as observed by fluorescence imaging. *C*, exposed popliteal lymph node. *Dotted lines*, area of lymphatic with trafficking cancer cells shown at high magnification in (*D*). *D*, fluorescence image of trafficking HT-1080 dual-color cells in the lymphatic denoted by dotted lines in (*C*). *Bar,* 10 mm (*A*); 1 mm (*B*); 2 mm (*C*); and 100 μm (*D*).

tumor, the number of single cells shed increased compared with no stimulation (Fig. 5*A* and *B*). With 250-g stimulation, the total cell number shed increased further and large emboli were seen (Fig. 5*C* and *D*; see Supplementary Movie 3). The number of cell fragments, cells, and emboli significantly increased with heavier stimulation (see Supplementary Table S1*A–C*). The maximum major axis of the trafficking emboli also increased with increased pressure (see Supplementary Table S1*D*). These data suggest that pressure in the tumor is important not only for the number of cells shed but also for the size of emboli shedding into lymphatics around the tumor. The larger emboli could have more possibility to survive and form a metastasis in the lymph node (28).

In this study, real-time cellular imaging of trafficking in lymphatic vessels in live mice was achieved with cancer cells expressing GFP in the nucleus and RFP in the cytoplasm or with RFP or GFP only. Contrast was achieved by labeling the lymphatic vessels and lymph nodes with FITC dextran. We were also able to image the entrance of cancer cells to the lymph node. Tumor cells may differ in lymphangiogenesis, migration to the peritumoral lymphatics, trafficking in lymphatic vessels, survival at the lymph node, migration in the lymph node, and growth in the lymph node, all of which are factors in lymph node metastasis. With the technology described in this report, all of these steps can be imaged in live animals. With increasing external weight put on the tumor to increase the internal pressure of the tumor, increased tumor-cell shedding and lymphatic trafficking was observed. This result might explain why high IFP is associated with poor prognosis in human cancer (4, 21, 22). For example, Rofstad et al. (23) reported that high central tumor IFP was found to be associated with the development of pulmonary and lymph node metastases. Increased cancer cell trafficking associated with increased IFP could increase the probability of metastasis. In this study, not only the number but also the size of emboli increased with increasing pressure. Larger emboli may have a higher probability to survive at a distant metastatic site.

Jain et al. stated that there are no functional lymphatic vessels inside solid tumors and functional lymphatic vessels are present only at the tumor margin and in the peritumoral tissue (29–31). Real-time imaging, such as that reported in the present study, could determine functionality of lymphatics with regard to the extent of cancer cell trafficking.

Increased IFP also leads to a decreased uptake of drugs. In 1987, Jain (32) hypothesized that the IFP in tumors must be high and serves as a barrier to efficient drug delivery. It is also known that increased IFP contributes to decreased transcapillary transport in tumors, presenting a potential obstacle to the uptake of agents for treatment (18).

Several types of treatment have been shown to decrease tumor IFP in animal models and patients, such as VEGF antagonists, platelet-derived growth factor antagonists, transforming growth factor-β antagonists, and tumor necrosis factor-α (18). The imaging model described in this report could determine if these drugs also reduced tumor-cell shedding.

Conclusions

We have developed fluorescence real-time cell imaging of lymphatic trafficking by means of fluorescent dual-color cancer cells and a high-resolution, real-time, small-animal imaging system. The imaging technology visualized the extent of cancer intralymphatic trafficking and lymph node targeting, differential intralymphatic cell viability, and the effect of pressure on tumor cells shedding into lymphatics. Internal pressure in the tumor is important not only for the number of cells shed into the lymphatics but also for the size of emboli shedding into lymphatic channels around the tumor. Tumor shedding was readily imaged using the labeled cancer cells and the real-time imaging system. The reason for increased IFP in tumors is not clear. It could be due to pressure

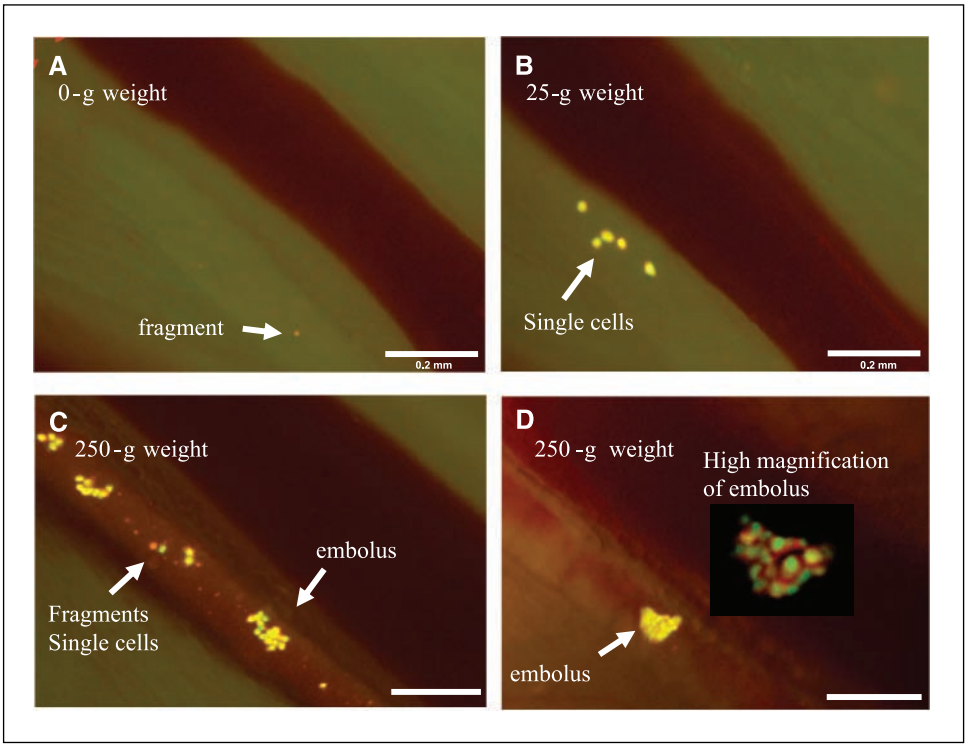

Figure 5. Effect of tumor pressure on tumor-cell shedding in lymphatic vessels. The footpad tumor was stimulated by 25- or 250-g weight for 10 s each to increase the internal pressure of the tumor. Stimulations were conducted on the same mouse with a minimum 5-min interval. A cylindrical weight with a 10-mm diameter (78.5 mm^2) was used for the stimulation. After stimulation, video rate imaging was done of cancer cell trafficking in the lymphatic vessel with the Olympus OV100 system at ×100 magnification for 1 min. The numbers of cell fragments, single cells, and emboli shed into the lymphatic vessel were counted by reviewing the saved movie files. The major axis of the maximum-size shed embolus in each experiment was also measured. *A,* no weight stimulation onto the footpad. There are only a few fragmented cells in the lymph duct. *B,* after a 10-s stimulation with a 25-g weight on the footpad, single cells as well as cell fragments are observed trafficking in the lymph duct. *C* and *D,* after a 10-s stimulation with the 250-g weight on the footpad, more cell emboli, single cells, and fragments were shed in the lymph duct. Dual-color cell was useful to distinguish the cell condition. *D*, a high magnification image of the embolus is also shown. *Bar*, 200 μm (*A–D*).

build-up due to insufficient lymphatic fluid drainage. This may lead to increased tumor-cell shedding into the lymphatics that are present in the tumor that can serve as a conduit for the tumor cells to metastasize to lymph nodes. Further imaging studies should increase our understanding of this phenomenon. Our imaging technology, therefore, can image the individual steps of lymphatic metastasis in real time.

Acknowledgments

Received 4/3/2007; revised 5/18/2007; accepted 7/6/2007.

Grant support: National Cancer Institute grants CA099258 and CA103563 (AntiCancer, Inc.) and NIH grant R21 CA109949-01 and American Cancer Society grant RSG-05-037-01-CCE (M. Bouvet).

The costs of publication of this article were defrayed in part by the payment of page charges. This article must therefore be hereby marked *advertisement* in accordance with 18 U.S.C. Section 1734 solely to indicate this fact.

References

1. Nathanson SD. Insights into the mechanisms of lymph node metastasis. Cancer 2003;98:413–23.
2. Hoshida T, Isaka N, Hagendoorn J, et al. Imaging steps of lymphatic metastasis reveals that vascular endothelial growth factor-C increases metastasis by increasing delivery of cancer cells to lymph nodes: therapeutic implications. Cancer Res 2006;66:8065–75.
3. Padera PT, Kadambi A, Tomaso E, et al. Lymphatic metastasis in the absence of functional intratumor. Science 2002;296:1883–6.
4. Gunn MD, Kyuwa S, Tam C, et al. Mice lacking expression of secondary lymphoid organ chemokine have defects in lymphocyte homing and dendritic cell localization. J Exp Med 1999;189:451–60.
5. Miller MJ, Wei SH, Cahalan MD, Parker I. Autonomous T cell trafficking examined *in vivo* with intravital two-photon microscopy. Proc Natl Acad Sci U S A 2003;100:2604–9.
6. Hoffman RM. The multiple uses of fluorescent proteins to visualize cancer *in vivo*. Nat Rev Cancer 2005;5:796–806.
7. von Andrian UH, Mempel TR. Homing and cellular traffic in lymph nodes. Nat Rev Immunol 2003;3:867–78.
8. Halin C, Rodrigo Mora J, Sumen C, von Andrian UH. *In vivo* imaging of lymphocyte trafficking. Annu Rev Cell Dev Biol 2005;21:581–603.
9. Stoll S, Delon J, Brotz TM, Germain RN. Dynamic imaging of T cell-dendritic cell interactions in lymph nodes. Science 2002;296:1873–6.
10. Dadiani M, Kalchenko V, Yosepovich A, et al. Real-time imaging of lymphogenic metastasis in orthotopic human breast cancer. Cancer Res 2006;66:8037–41.
11. Jain RK, Munn LL, Fukumura D. Dissecting tumour pathophysiology using intravital microscopy. Nat Rev Cancer 2002;2:266–76.
12. Young JS, Lumsden CE, Stalker AL. The significance of the tissue pressure of normal testicular and of neoplastic (Brown-Pearce carcinoma) tissue in the rabbit. J Pathol Bacteriol 1950;62:313–33.
13. Less JR, Posner MC, Boucher Y, et al. Interstitial hypertension in human breast and colorectal tumors. Cancer Res 1992;52:6371–4.
14. Nathanson SD, Nelson L. Interstitial fluid pressure in breast cancer, benign breast conditions, and breast parenchyma. Ann Surg Oncol 1994;1:333–8.
15. Curti BD, Urba WJ, Alvord WG, et al. Interstitial pressure of subcutaneous nodules in melanoma and lymphoma patients: changes during treatment. Cancer Res 1993;53:2204–7.
16. Boucher Y, Kirkwood JM, Opacic D, Desantis M, Jain RK. Interstitial hypertension in superficial metastatic melanomas in humans. Cancer Res 1991;51:6691–4.
17. Gutmann R, Leunig M, Feyh J, et al. Interstitial hypertension in head and neck tumors in patients: correlation with tumor size. Cancer Res 1992;52:1993–5.
18. Heldin CH, Rubin K, Pietras K, Ostman A. High interstitial fluid pressure—an obstacle in cancer therapy. Nat Rev Cancer 2004;4:806–13.
19. Hagendoorn J, Tong R, Fukumura D, et al. Onset of abnormal blood and lymphatic vessel function and interstitial hypertension in early stages of carcinogenesis. Cancer Res 2006;66:3360–4.
20. Padera TP, Stoll BR, Tooredman JB, et al. Pathology: cancer cells compress intratumour vessels. Nature 2004;427:695.
21. Roh HD, Boucher Y, Kalnicki S, et al. Interstitial hypertension in carcinoma of uterine cervix in patients: possible correlation with tumor oxygenation and radiation response. Cancer Res 1991;51:6695–8.
22. Milosevic M, Fyles A, Hedley D, et al. Interstitial fluid pressure predicts survival in patients with cervix cancer independent of clinical prognostic factors and tumor oxygen measurements. Cancer Res 2001;61:6400–5.
23. Rofstad EK, Tunheim SH, Mathiesen B, et al. Pulmonary and lymph node metastasis is associated with primary tumor interstitial fluid pressure in human melanoma xenografts. Cancer Res 2002;62:661–4.
24. Yamauchi K, Yang M, Jiang P, et al. Real-time *in vivo* dual-color imaging of intracapillary cancer cell and nucleus deformation and migration. Cancer Res 2005;65:4246–52.
25. Yamauchi K, Yang M, Jiang P, et al. Development of real-time subcellular dynamic multicolor imaging of cancer cell trafficking in live mice with a variable-magnification whole-mouse imaging system. Cancer Res 2006;66:4208–14.
26. Kanda T, Sullivan KF, Wahl GM. Histone-GFP fusion protein enables sensitive analysis of chromosome dynamics in living mammalian cells. Curr Biol 1998;8:377–85.
27. Yamamoto N, Jiang P, Yang M, et al. Cellular dynamics visualized in live cells *in vitro* and *in vivo* by differential dual-color nuclear-cytoplasmic fluorescent-protein expression. Cancer Res 2004;64:4251–6.
28. Thompson SC. The colony-forming efficency of single cells and cell aggregates from a spontaneous mouse mammary tumour using the lung colony assay. Br J Cancer 1974;30:332–6.
29. Fukumura D, Jain RK. Tumor microenvironment abnormalities: causes, consequences, and strategies to normalize. J Cell Biochem 2007;101:937–49.
30. Jain RK, Fenton BT. Intratumoral lymphatic vessels: a case of mistaken identity or malfunction? J Natl Cancer Inst 2002;94:417–21.
31. Ji RC. Lymphatic endothelial cells, tumor lymphangiogenesis and metastasis: new insights into intratumoral and peritumoral lymphatics. Cancer Metastasis Rev 2006;25:677–94.
32. Jain RK. Transport of molecules across tumor vasculature. Cancer Metastasis Rev 1987;6:559–93.